ADVANCED MATERIALS
www.advmat.de

Electric-Field Control of the Local Thermal Conductivity in Charge Transfer Oxides

*Noa Varela-Domínguez, Marcel S. Claro, Carlos Vázquez-Vázquez, Manuel Arturo López-Quintela, and Francisco Rivadulla**

Phonons, the collective excitations responsible for heat transport in crystalline insulating solids, lack electric charge or magnetic moment, which complicates their active control via external fields. This presents a significant challenge in designing thermal equivalents of basic electronic circuit elements, such as transistors or diodes. Achieving these goals requires precise and reversible modification of thermal conductivity in materials. In this work, the continuous tuning of local thermal conductivity in charge-transfer $SrFeO_{3-x}$ and $La_{0.6}Sr_{0.4}CoO_{3-x}$ oxides using a voltage-biased Atomic Force Microscopy (AFM) tip at room temperature is demonstrated. This method allows the creation of micron-sized domains with well-defined thermal conductivity, achieving reductions of up to 50%, measured by spatially resolved Frequency Domain Thermoreflectance (FDTR). By optimizing the oxide's chemical composition, the thermal states remain stable under normal atmospheric conditions but can be reverted to their original values through thermal annealing in air. A comparison between Mott–Hubbard and charge-transfer oxides reveals the critical role of redox-active lattice oxygen in ensuring full reversibility of the process. This approach marks a significant step toward fabricating oxide-based tunable microthermal resistances and other elements for thermal circuits.

1. Introduction

So far, most of the strategies for the reversible control of the thermal conductivity exploited the reversibility of structural phase transitions,[1–3] the natural interfaces of ferroelectrics,[4–7] or the accumulation of mobile defects at interfaces.[8]

Recently, the electric field control over the topotactic exchange of O^{2-} and H^{+} in $(La,Sr)CoO_x$ through ionic-liquid electrochemical gating was used for reversible modulation of its thermal conductivity, at room temperature.[9,10] In this case, the strong covalency between the $Co^{3+/4+}$ redox pair and O 2p results in a partially filled wide σ^* band, which provides the required conductivity for the electrodes of the electrochemical cell, and reduces the enthalpy of oxygen vacancy formation and migration.[11] However, apart from how impractical the use of ionic liquids may be, O^{2-} ions are the redox active species in Co oxides at high oxidation states, which results in an intrinsic chemical instability that leads to corrosion and dissolution of the films, and partial irreversibility and reproducibility issues.[9] By using the solid electrolyte $Y:ZrO_2$, Yang et al.[12] overcome this unwanted effect and achieve a reversible transition in $SrCoO_{3-x}$, with good repeatability and a reproducible κ(ON/OFF) ≈4. However, the need for high temperatures (≈300 °C) to reach sufficient oxygen mobility, and the required solid electrolyte/oxide architecture, can be a drawback for some applications.

Here, we demonstrate that the local thermal conductivity of transition-metal perovskite oxide thin films can be precisely defined by a voltage-biased Atomic Force Microscopy (AFM) tip, at room temperature, under ambient conditions.

It has been previously shown by other authors that the strongly localized electric field exerted by a voltage-biased AFM tip on the surface of a material can be used to modify its properties, permanently, through an electrochemical reaction, or transiently, by controlling the local charge density.[13] In the first case, the humidity of the atmosphere may supply enough H_2O molecules to form a meniscus between the apex of the tip and the surface of the sample, which works as a localized micro-electrolytic cell. The electric field splits the water molecules in strongly oxidizing species, producing the electrodeposition of an oxide on the surface through local anodic oxidation.[14,15] This constitutes a sort of AFM-lithography, which has been used to modify, permanently, the local surface in semiconductors and to fabricate non-volatile functional nanostructured devices, with excellent spatial resolution.[16–19]

N. Varela-Domínguez, M. S. Claro, F. Rivadulla
Centro Singular de Investigación en Química Biolóxica e Materiais Moleculares (CIQUS)
Departamento de Química-Física
Universidade de Santiago de Compostela
Santiago de Compostela 15782, Spain
E-mail: f.rivadulla@usc.es

C. Vázquez-Vázquez, M. A. López-Quintela
Instituto de Materiales (iMATUS)
Departamento de Química-Física
Universidade de Santiago de Compostela
Santiago de Compostela 15782, Spain

The ORCID identification number(s) for the author(s) of this article can be found under https://doi.org/10.1002/adma.202413045

DOI: 10.1002/adma.202413045

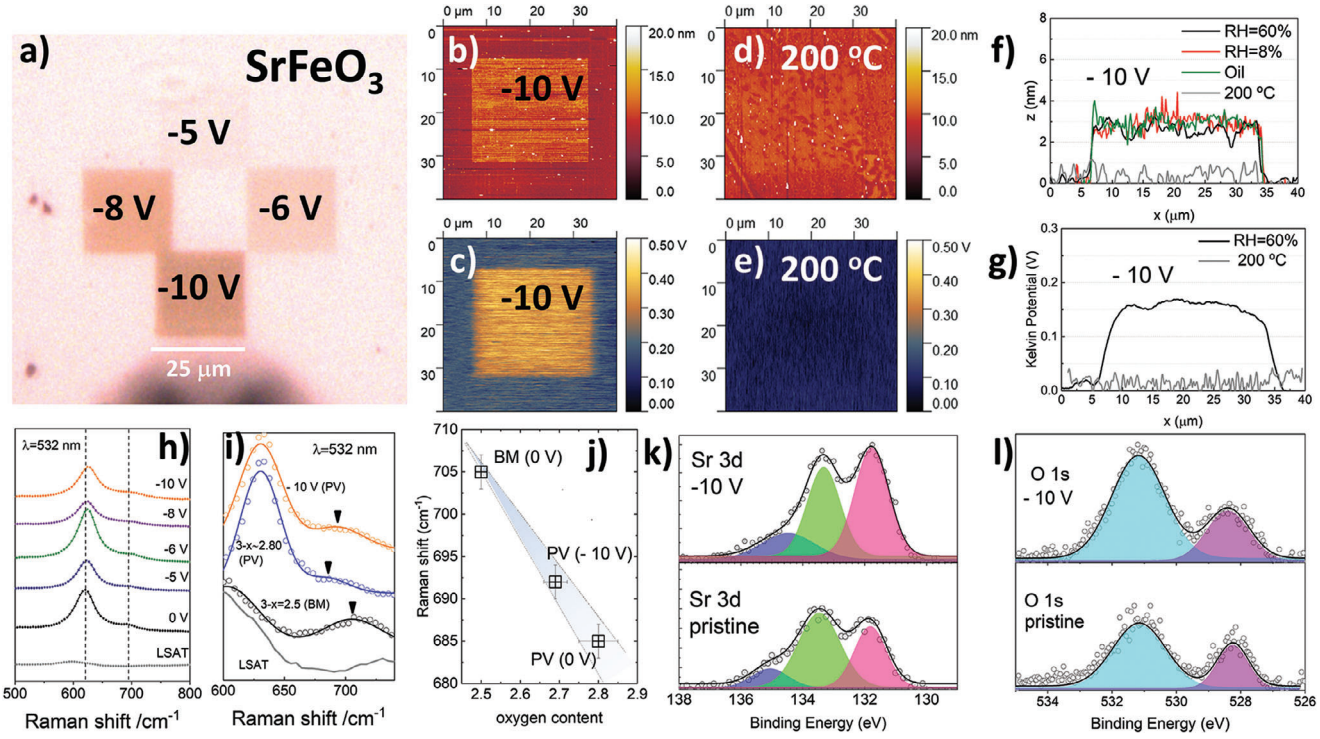

Figure 1. Effect of local electric field on negative charge-transfer oxide $SrFeO_{3-x}$. a) Optical image (reflected light) of four pads of 25 × 25 μm^2 scanned with the AFM tip biased at different voltages on the surface of PV $SrFeO_{3-x}$ film. b) Topography and c) Kelvin potential probe scans of the −10 V pad. The topography and Kelvin repeated on the same area after annealing the sample in the air at 200 °C are shown in d) and e), respectively. f) Height and g) Kelvin potential line profiles along the pads at − 10 V. The line scans of the topographies done under 8% relative humidity, immersed in mineral oil, and after thermal annealing, are also shown for comparison. h) Evolution of the Raman spectrum around the ≈630 cm^{-1} signal with the applied voltage. The films are deposited on LSAT substrates for the Raman experiments. i) Comparison of the Raman spectra of a $SrFeO_{3-x}$ film on the PV phase (3−x ≈ 2.80(5)), the BM phase (3−x ≈ 2.5) and on a region of the film scanned at −10 V. The spectra were fitted with two Gaussian functions (solid lines). The spectrum of the LSAT substrate is also shown. j) Oxygen content of the region scanned at −10 V, estimated from the linear dependence of the ≈700 cm^{-1} Raman peak between the BM and the pristine PV (3−x ≈ 2.8). k,l) Sr 3d and O 1s XPS spectra of the film taken on the bare surface and the region scanned at −10 V. There is a small increase in the relative intensity of the lower binding energy peak of Sr 3d, consistent with a Sr-poor surface after application of the electric field. In the O 1s spectra the purple and cyan bands identify the contribution from lattice oxygen and mixed hydroxide groups, respectively.

On the other hand, a voltage-biased AFM tip was also used for tuning the local concentration of HO^-/H^+ surface adsorbates on the top layer of an $LaAlO_3/SrTiO_3$ interface, influencing the conductance of the interfacial 2D electron gas. Different types of functional devices were fabricated in this way, although the effect normally vanishes after a few hours under atmospheric conditions.[20–22]

Here, we employ a voltage-biased AFM tip to establish non-volatile thermal states in charge-transfer transition-metal oxides. Optimizing the contribution of O 2p states at the Fermi Energy makes the thermal states stable for weeks, but they can be completely erased after thermal annealing, returning the system to its original state. This constitutes a novel application of AFM lithography to fabricate micron-size patterns with a defined value of thermal conductivity on the bare surface of the oxide thin film. Our results demonstrate that conductive AFM-driven ionic manipulation is a promising technology for the design of the elements of a thermal circuit.

2. Results and Discussion

2.1. Effect of Local Electric Field on the Surface of $SrFeO_{3-x}$, $La_{0.6}Sr_{0.4}CoO_{3-x}$ and $La_{0.7}Sr_{0.3}MnO_3$

We have scanned several regions (25 × 25 μm^2) of the surface of 40 nm thick $SrFeO_{3-x}$ (SFO) films with a voltage-biased AFM tip, at a relatively fast scan rate of 0.5 Hz (12.5 μm s^{-1}). This speed (the total amount of charge injected into the sample) was optimized for achieving a compromise between stability and reversibility of the effect of the electric field on the surface of the films, as explained in the rest of the paper (see Figure S1, Supporting Information for further details about the effect of a larger electric field on the surface of $SrFeO_x$).

Increasing the (negative) voltage above −5 V produces a darkening of the film surface, appreciable in the optical image (**Figure 1a**), and an increase of the height and local surface potential (Figure 1b,c), which grow linearly with the voltage. The local accumulation of oxygen vacancies, $V_{\ddot{O}}$, by the electric field

may produce a structural transformation to brownmillerite, BM, $SrFeO_{2.5}$, with an associated change in the electrical and optical conductivity.[23–25] However, the full transformation of a 40 nm film of perovskite (PV, c = 3.852 Å) to BM (c = 3.985 Å) will imply a maximum expansion of ≈1.3 nm, well below the ≈3 nm observed at −10 V; Figure 1f.

On the other hand, every $V_{Ö}$ in the perovskite donates two electrons to nonbonding orbitals, resulting in the expansion of the crystalline lattice.[26] In the case of epitaxial thin films, this effect may be strongly anisotropic, resulting in a much larger expansion.[27]

Quantifying the precise amount of oxygen vacancies introduced in the written pads is an extremely difficult task, due to the small dimension of these regions. However, an approximate estimation of the maximum number of vacancies created by the electric field can be obtained from the analysis of the Raman spectra (Figure 1h,i). The peaks at ≈630 and ≈700 cm^{-1} in the pristine PV could be assigned to different Fe-O stretching modes, both absent in the bulk brownmillerite phase due to symmetry constraints.[28,29] However, the peak at ≈700 cm^{-1} is still present with a large intensity in the epitaxial BM, signaling some symmetry relaxation in the film (Figure 1i). Moreover, epitaxial clamping introduces restrictions in the vibrational modes, which along with the stress relaxation for accommodating the oxygen vacancies, or even vacancy ordering or clustering, could lead to the observed hardening of the Raman modes associated with Fe–O stretching. Assuming a linear variation of the frequency with the oxygen composition between the BM (3-x ≈ 2.5) and the pristine PV (3-x ≈ 2.82(5)),[23,30] this would place the oxygen content in the pads written at − 10 V at about 3-x≈2.68(2) (Figure 1j). This is an approximate value of the maximum reduction we can achieve with our method while maintaining the PV structure (see also Figure S1, Supporting Information).

On the other hand, the effect of the electric field on the chemical composition of the surface was studied by X-ray Photoelectron Spectroscopy (XPS). The changes observed in the Fe 2p XPS spectra are negligible (Figure S2, Supporting Information). Regarding the O 1s spectrum (Figure 1l), apart from the contribution from lattice oxygen, there is a signal which can be attributed to hydroxide groups,[31,32] but no significative changes are observed after the application of the electric field. Minimum changes are also observed in the relative intensities of the Sr 3d multiplet (Figure 1k) which could be related to a slight decrease of surface Sr on the area of the film scanned at −10 V.[32,33]

Therefore, the analysis of the XPS spectra discards the electrodeposition of an oxide or oxohydroxide by the effect of the electric field. To further discard the role of adsorbed H_2O in the surface expansion, the experiments were repeated after reducing the relative humidity below 8%, and also after immersing the AFM cantilever and the film surface in mineral oil. In both cases, the local surface expansion remains ≈ 3 nm at −10 V (see Figure 1f; Figure S3, Supporting Information). These experiments confirm an intrinsic origin of the local surface expansion, not related to an electrochemical reaction with adsorbed water.

Understanding the effect of the electric field on the surface of the film requires a detailed consideration of the electronic structure of these oxides: increasing enough the oxidation state of Fe as in $SrFeO_{3-x}$, reduces the energy of the σ^* band derived from the Fe-O antibonding interaction below the non-bonding O 2p states. This makes the charge-transfer energy, $\Delta = [E(M^{3+}L) - E(M^{4+})]$, negative and stabilizes a $Fe^{3+}L$ (L meaning a ligand-hole), rather than a pure Fe^{4+} ground state.[34–36] Therefore, there will be a strong contribution of O 2p states at the Fermi energy and oxidation of the lattice O^{2-} will compete with the oxidation of Fe^{3+}. Therefore, the electric field will not only drag and cluster the existing oxygen vacancies in the film but will also increase their amount through local oxidation of the O^{2-} ion, which will be released as O_2. We hypothesize that the accumulation of oxygen vacancies may explain the enhanced surface expansion since it induces a large anisotropic chemical expansion in these materials when they are strained.[27,37] The accumulation of oxygen vacancies may result in the stabilization of lower symmetry phases which may also contribute further to this expansion. As shown in Figure 1d–g, annealing the film at 200 °C in the air is enough to reincorporate the oxygen back to the structure, returning the oxide to the original state.

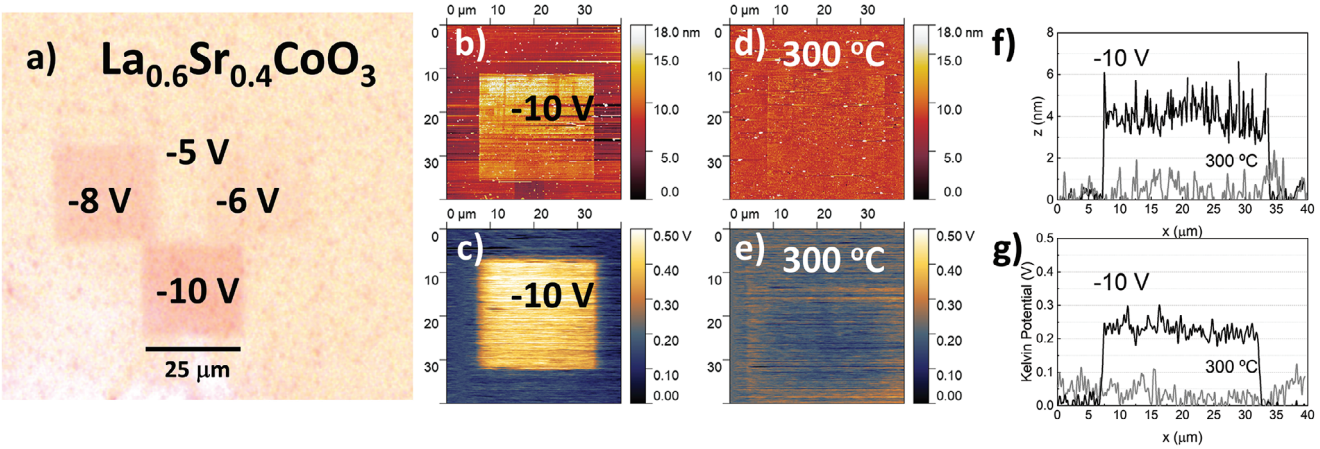

Figure 2. Effect of local electric field on charge-transfer oxide $La_{0.6}Sr_{0.4}CoO_3$. a) Optical image (reflected light) of four pads of 25 × 25 $µm^2$ scanned with the AFM tip biased at different voltages on the surface of PV LSCO film. b) Topography and c) Kelvin potential probe scans of the −10 V pad. The topography and Kelvin repeated on the same area after annealing the sample in the air at 300 °C are shown in d) and e), respectively. f) Height and g) Kelvin potential line profiles along the pads at −10 V, and after the thermal annealing.

Note that this mechanism of local O^{2-} oxidation should be active in other charge transfer oxides, but not in those of the Mott–Hubbard type, in which the transition-metal ion is the active redox pair (see Figure S4, Supporting Information).

To verify this hypothesis, we scanned the surface of charge-transfer $La_{0.6}Sr_{0.4}CoO_3$ (LSCO) and Mott–Hubbard $La_{0.7}Sr_{0.3}MnO_3$ (LSMO).[38] The results are shown in **Figures 2** and **3**. Similar to SFO, the application of the electric field on the surface of charge-transfer LSCO produces a maximum expansion of ≈3–4 nm at −10 V; this effect can be reversed by annealing the film at 300—350 °C in air; Figure 2.

However, the effect of the electric field is completely different in the Mott–Hubbard oxide LSMO; Figure 3. The surface expansion in this material reaches ≈15 nm at −10 V in a 40 nm film, and cannot be completely reversed by annealing in air, even at 500 °C. The difference is also appreciated in the XPS spectrum: the O 1s signal shows four different components, including lattice oxygen (purple), surface termination component (blue), oxy-hydroxide lattice oxygen (orange), and mixed hydroxide groups (cyan).[32] As shown in Figure 3g), the electric field increases the signal from the hydroxide groups at the expense of the oxygen lattice contribution. In the case of La $3d_{5/2}$, there is a shift in binding energy after application of -10 V, and the splitting of the La $3d_{5/2}$ multiplet reduces from 4.53 eV at the pristine surface to 3.9 eV at −10 V. Both observations are remarkably similar to the effects observed after surface reconstruction of $La_{0.6}Sr_{0.4}CoO_3$ catalyst during OER operation conditions.[32] Therefore, the XPS data indicate the electrodeposition of La and Mn hydroxide/oxo-hydroxide species on the surface of LSMO, by an electrochemical reaction with the adsorbed water, similar to the irreversible oxidation of the surface of Si by AFM nanolithography.[14] Immersing the LSMO in mineral oil suppresses this mechanism, which reduces the expansion to ≈5 nm (Figure 3e). Note that although small, the participation of the O 2p band in the redox process cannot be completely eliminated in these oxides, and in the absence of ambient humidity the oxidation of lattice oxygen is responsible for the surface expansion. Therefore, the action of a voltage-biased AFM tip on the bare surface of LSMO, under normal atmospheric conditions, is the combination of electrostatic attraction of $V_{\ddot{O}}$ and electrochemical modification of its surface.

In summary, our results demonstrate that it is possible to modify the concentration of $V_{\ddot{O}}$ by the application of an electric field by a voltage-biased AFM tip resulting in a non-volatile increase of the local surface height. Optimizing the contribution of O 2p states to the Fermi Energy and the scan rate, it is possible to make this effect reversible after thermal annealing in air.

Next, we will show how this AFM lithography can be exploited to manipulate the thermal conductivity, creating non-volatile thermal states with micron size resolution.

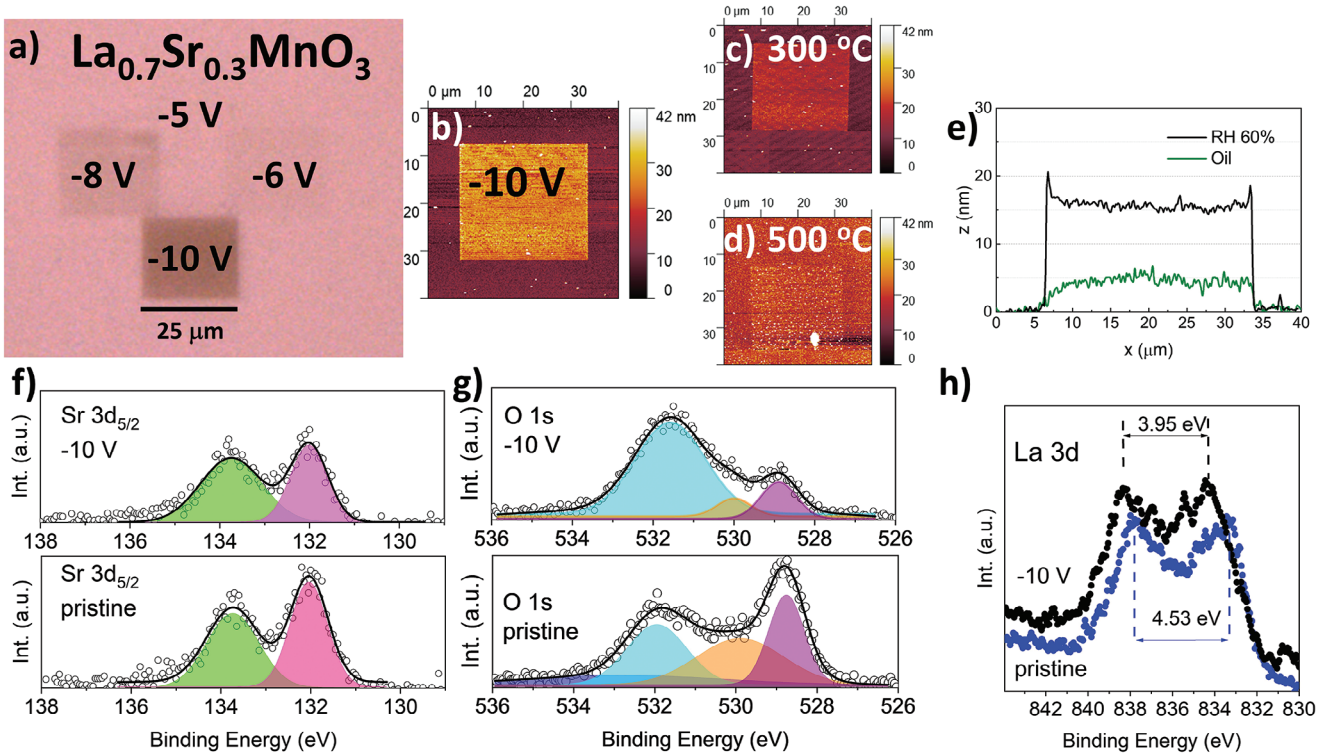

Figure 3. Effect of local electric field on Mott–Hubbard oxide $La_{0.7}Sr_{0.3}MnO_3$. Optical image (reflected light) of four pads of 25 × 25 μm² scanned with the AFM tip biased at different voltages. The AFM topography of one pad written at −10 V is shown in b). c,d) Show the topography of the same area after annealing at 300 and 500 °C, respectively, demonstrating the irreversibility of the surface transformation in this case. The height line profile along this pad is shown in e). We included the height profile of the sample scanned in the absence of humidity (immersed in mineral oil), for comparison. f–h) Sr 3d, O 1s, and La $3d_{5/2}$ XPS spectrum of the film taken on the pristine surface and on the region scanned at −10 V. The changes observed in the O 1s and La 3d spectra are consistent with the formation of an oxo-hydroxide species on the surface of the film, pointing to a local electrochemical reaction with adsorbed water (see text).

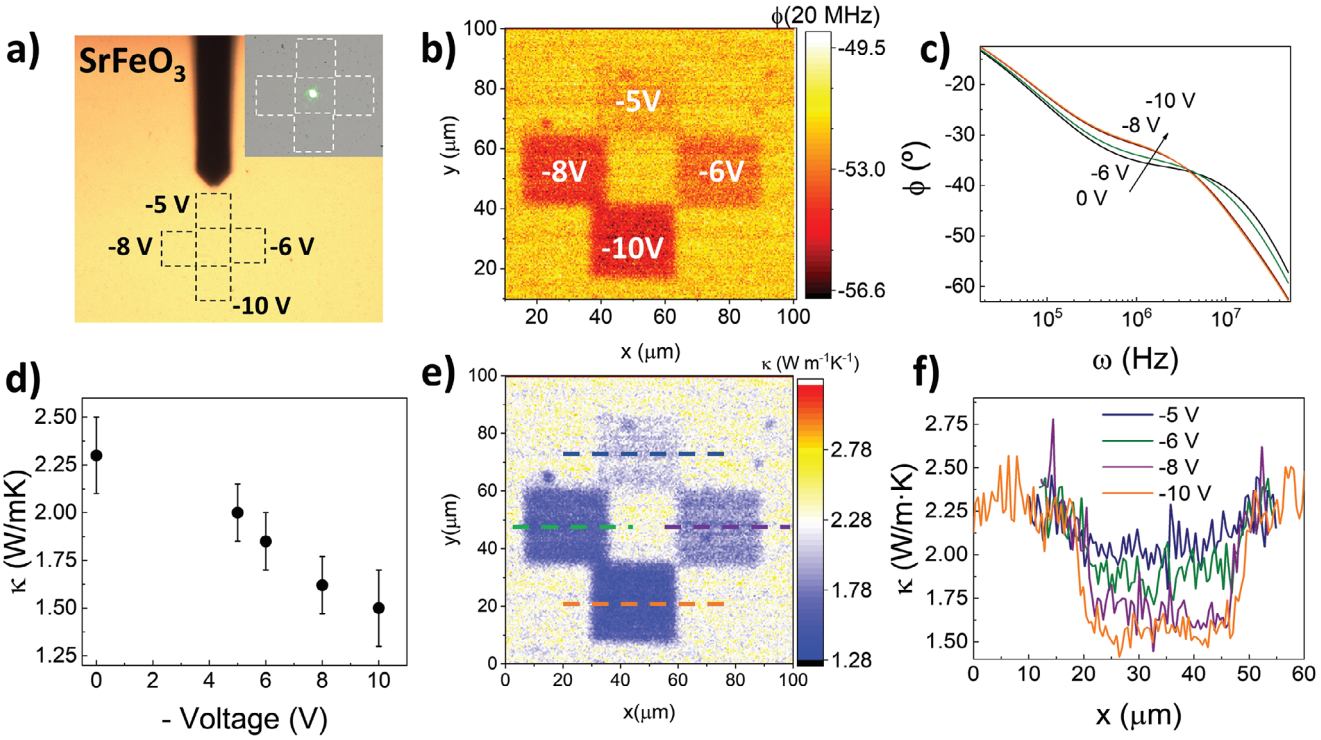

Figure 4. Electric-field control of local thermal conductivity in $SrFeO_{3-x}$. a) Optical image of the surface of a 40 nm thick SFO film, previously scanned with a voltage-biased AFM tip, covered with 60 nm of Au for the FDTR measurements. The written pads (like those shown in Figure 1a) are not visible across the Au layer, but their approximate positions are indicated as dashed squares. The shadow of the AFM cantilever is visible in the image. The inset shows an image of the same region of the surface from the FDTR camera, with the spot of the probe laser beam in the center. b) Phase shift map at 20 MHz obtained scanning a region of 100 × 100 μm^2, 0.5 μm step, with the pump/probe laser beams. The four regions scanned with the AFM tip are now visible in the phase-shift map. Phase versus frequency curves were taken inside each of these regions (c), showing a clear evolution with the voltage applied. Fitting to a thermal model (see text) gives the local thermal conductivity, which decreases linearly with the voltage, as shown in (d). e) Thermal conductivity map obtained by fitting the phase-shift map at 20 MHz, where the sensitivity to the thermal conductivity of the film is maximized. Line scans along different directions of the map, f), show the excellent control over the local thermal conductivity achieved by this method.

2.2. Electric-Field Modulation of the Local Thermal Conductivity of $SrFeO_{3-x}$, $La_{0.6}Sr_{0.4}CoO_{3-x}$ and $La_{0.7}Sr_{0.3}MnO_3$

Spatially-resolved (micron-size resolution) thermal conductivity, κ, of the films was measured by Frequency Domain Thermoreflectance (FDTR).[39] A 60 nm thick layer of Au was sputtered on the surface of the film, to serve as a thermal transducer. The thermal properties of the sample are determined through multi-parameter fitting of the phase lag of the pump/probe lasers, $\phi(\omega)$, as explained in reference.[39] The different parameters of the model were measured independently or obtained from the literature, so that κ of the film is the only fitting parameter (see Table S1 and Figure S5, Supporting Information for further details of the fittings). The main results of this analysis are shown in **Figure 4** for $SrFeO_{3-x}$.

Once covered with 60 nm of Au, the contrast from the pattern written with the electric field on the surface of SFO is no longer visible (Figure 4a). Therefore, we scanned a region of 100 × 100 μm^2, with a step of 0.5 μm, recording the $\phi(\omega)$ at six different frequencies, chosen for maximum sensitivity to κ (see Figure S5, Supporting Information for the sensitivity analysis). The four regions previously scanned with the voltage-biased AFM tip become perfectly visible in the ϕ (20 MHz) map shown in Figure 4b. In Figure 4c we show four $\phi(\omega)$ curves recorded inside the written areas, showing the change in the raw data with the applied electric field. Fitting the $\phi(\omega)$ shows the linear reduction of κ above −5 V, until a maximum reduction of ≈ 33% at −10 V (Figure 4d; Figure S6, Supporting Information). The electrical resistivity measured for $SrFeO_{3-x}$ is of the order of 0.05–0.1 Ω cm^{-1}, at room temperature, which accounts for a very small contribution (≈0.1 W m^{-1} K^{-1}) to the thermal conductivity. Therefore, the reduction of κ cannot be due to an increase of the electrical resistance by the effect of the electric field, but it must have its origin on the accumulation of point defects and its effect on the propagation of phonons.[40]

Maps of spatial distribution of κ were generated by fitting the $\phi(\omega)$ data points at every pixel to the thermal model. The maps and the line-scans shown in Figure 4e,f, demonstrate the excellent control over the local κ achieved by this method; sharp boundaries between the areas written under different voltages and the pristine film, can be perfectly defined.

Quantitatively similar reduction of the thermal conductivity was observed in films up to ≈70 nm thick. Given that the film thickness enters directly into the thermal model to fit the experimental $\phi(\omega)$ data, this confirms that the change induced by the voltage occurs through the film thickness, at least up to 70 nm, and it is not just a surface effect (see Figure S7, Supporting Information).

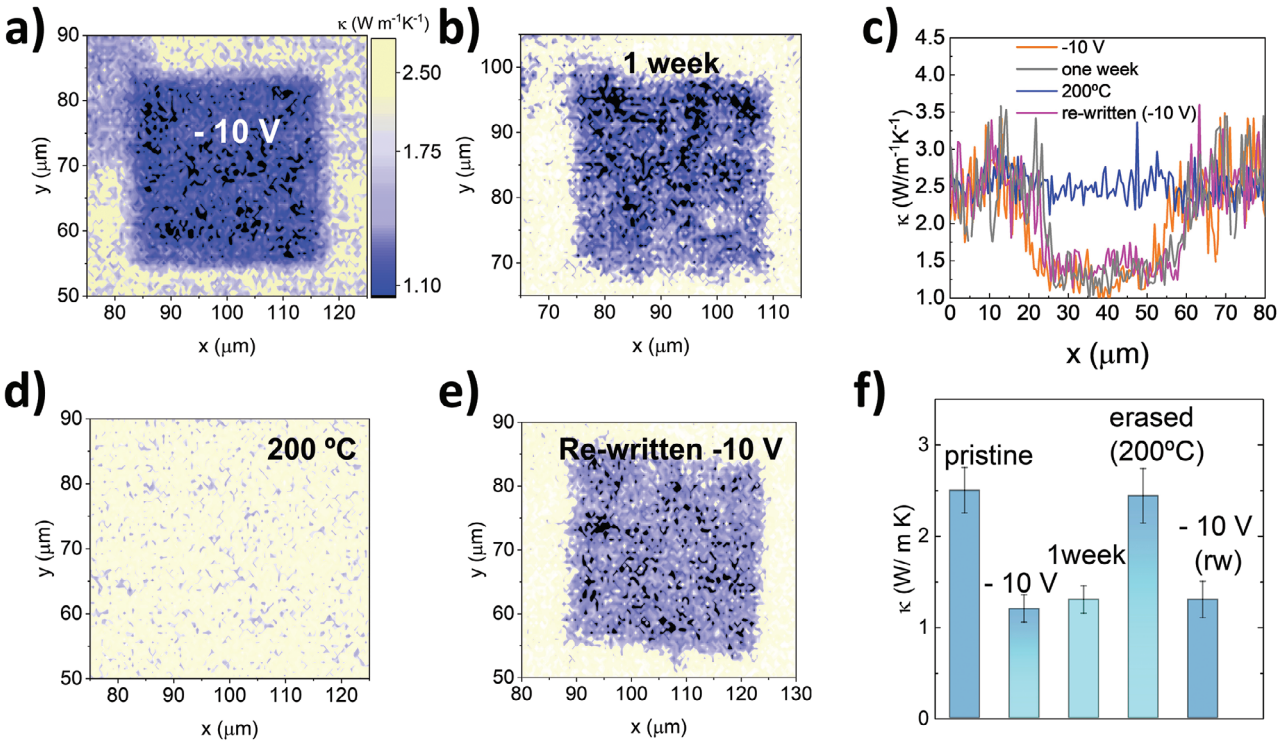

Figure 5. Stability and reversibility of the written thermal states in $SrFeO_{3-x}$. The stability of the thermal states has been probed by following the evolution of the area scanned at −10 V a), after one week under ambient conditions b), after being annealed in air at 200 °C d), and rewritten at −10 V in the same area of the film e). The line scans in c) and the histogram in f) show the local thermal conductivity after these processes, demonstrating the stability and reversibility of the process.

To probe the stability of the written thermal states, we followed their evolution under usual atmospheric conditions. In this case, the samples are not covered with Au until just before the FDTR experiments, to allow any possible oxygen exchange or sensitivity to ambient humidity. As shown in **Figure 5**, the thermal conductivity of the written areas is stable after several days but can be reversed to the original state by a gentle thermal annealing in air, above 200 °C, leaving it ready for a new process of electric-field writing. The results are similar for the samples written in the absence of humidity (Figure S8, Supporting Information).

A slightly larger reduction of the thermal conductivity can be achieved after full reduction to BM (Figure S1, Supporting Information), but the repeated structural transformation introduces defects and reduces the reversibility of the process.

In **Figure 6** we show the results for LSCO. Similar to SFO, thermal maps and line scans show a local reduction of κ proportional to the applied voltage, reaching a maximum reduction of ≈55% at −10 V.

The thermal states are also stable under ambient conditions and can be erased by thermal annealing, although in this case, the temperature must be higher than 350 °C for recovering the original surface state.

Finally, the results for Mott–Hubbard oxide LSMO are shown in **Figure 7**. Consistent with the large and irreversible modification of the surface observed in this material (see Figure 3), the reduction of κ at −10 V reaches 70%, but it is nonreversible. Actually, the thermal conductivity remains ≈30% lower than the original value after annealing the sample at 500 °C in air.

3. Conclusion

We have demonstrated that a voltage-biased AFM tip can write non-volatile thermal states with micron-size resolution in transition-metal oxide thin films at room temperature, under ambient conditions, and without further modification of the surface of the film. Optimizing the contribution of O 2p states to make the charge-transfer gap slightly negative, presents the optimum compromise of easy oxygen vacancy formation and stability, for continuous tunability and retention of the thermal states. The surface of the film can be restored by gentle heat treatment, so that the thermal states can be erased, and the material reused. The action of the conductive AFM tip over the bare surface of the film offers important practical advantages over liquid-electrochemical methods and avoids the inherent instability of the negative charge transfer oxides under anodic oxidation conditions in liquid media.

Therefore, the method presented in this paper constitutes the most precise for the control of the local thermal conductivity in oxides reported so far.

4. Experimental Section

Pulsed Laser Deposition of the Films: Thin films of $SrFeO_{3-x}$ (SFO), $La_{0.6}Sr_{0.4}CoO_{3-x}$ (LSCO) and $La_{0.7}Sr_{0.3}MnO_3$ (LSMO) were deposited on (0 0 1)-STO by PLD, at a temperature of 675 °C for SFO and LSCO, and 730 °C in the case of LSMO. All thin films were grown at an oxygen pressure of 100 mTorr, with laser fluence ≈ 1.5 J cm^{-2}.

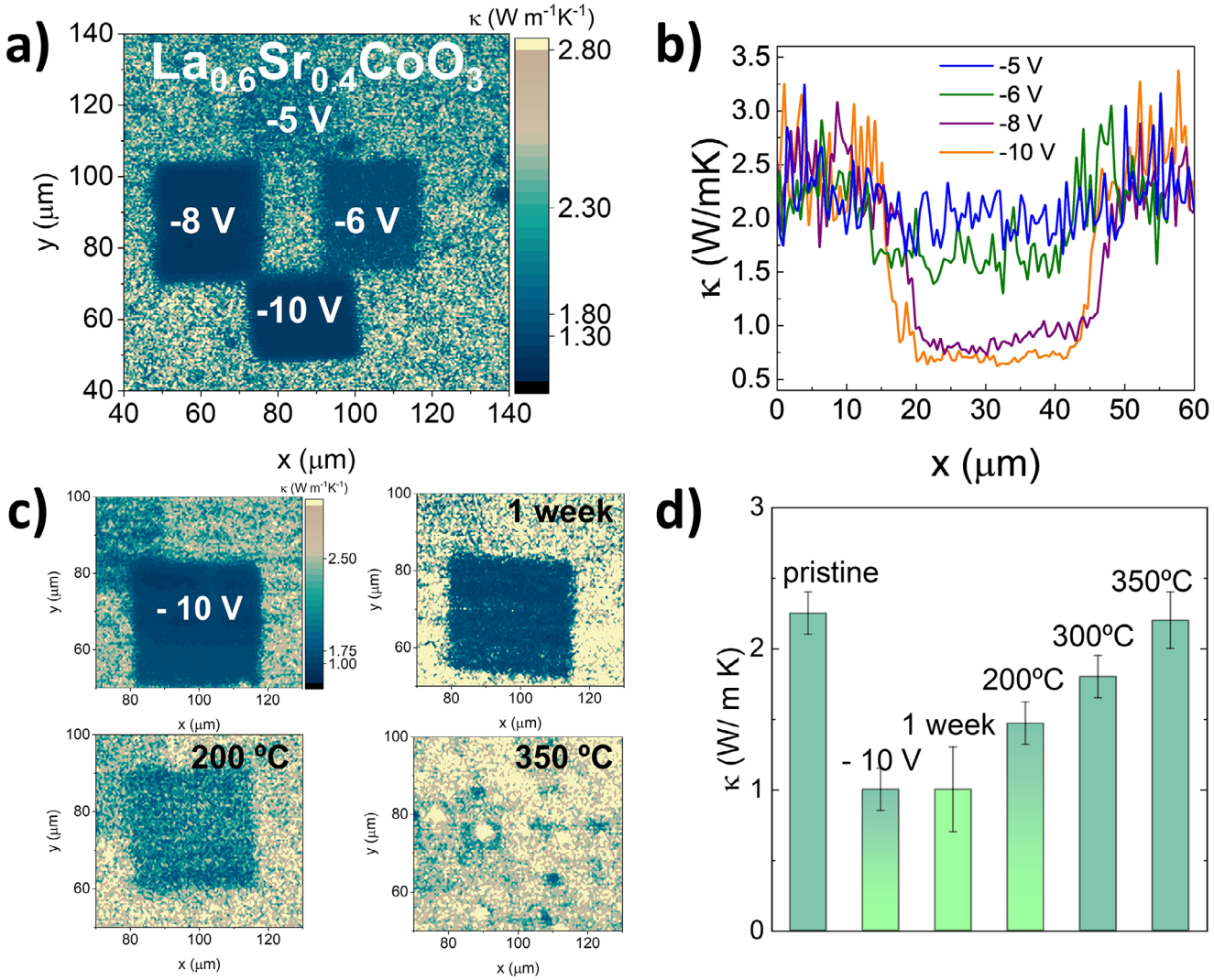

Figure 6. Electric-field control of local thermal conductivity in $La_{0.6}Sr_{0.4}CoO_{3-x}$. a) Thermal conductivity map of a LSCO film after scanning several areas of 25 × 25 μm^2 with a voltage-biased AFM tip. The map was obtained by fitting the phase-shift curves of the FDTR experiments to a thermal model, as explained in the text. Line scans of thermal conductivity along each pad are shown in b). c) Retention and reversibility of the written thermal states were probed by following the evolution of the −10 V pads, after 1 week under normal atmospheric conditions; after thermal annealing at 200 °C; after thermal annealing at 350 °C. The values after each treatment are shown in d). The states written at −10 V can be erased by annealing at 350 °C.

FDTR Measurements: The cross-plane thermal conductivity of the films was measured by Frequency Domain Thermoreflectance (FDTR).[39] A sinusoidally modulated pump laser ($\lambda = 488$ nm, modulating f = 2 kHz–50 MHz, spot sizes 1/e^2 radius ≈3.7 or 10.5 μm) was focused on the surface of the film, coated by a 60-nm-thick layer of Au, to produce an oscillatory modulation of the surface temperature. This results in a periodic variation of the Au thermoreflectance, which was probed by a laser beam ($\lambda = 532$ nm). The thermal properties of the sample were obtained by fitting the phase data to an analytical solution of the heat diffusion equation, in a multilayer model (see Supporting Information for further details).[39] The thermal conductivity of the substrates was obtained from Ref. [41] For Au, the electrical conductivity in co-deposited samples was measured and used the Wiedemann–Frantz law to obtain k_{Au}. The C_p of the substrate and Au transducer were measured or obtained from the literature.

In the FDTR experiment, when the thermal penetration depth is shorter than the spot size of the heating laser, the temperature profile in the film can be approximated by a steady-state 1D solution along its thickness, i.e., the cross-plane thermal conductivity was of particular sensitivity (thermal diffusivity of STO $\alpha \approx 3.5 \times 10^{-6}$ m^2 s^{-1}). To separate the effect of the thermal boundary conductance (TBC) on the absolute value of κ of the films, they were deposited over half of the substrate while the Au transducer covered the whole surface (film plus bare substrate). Fitting the data from the bare portion of the substrate the value for the Au/substrate TBC was obtained; this, in turn, can be used as an initial value for the Au/film TBC. The experiments were performed with two spot sizes (1/e^2 ≈ 3.7 and 10.5 μm).

Voltage-Biased AFM Transformations: AFM experiments were performed on a NX10 by Park Systems, using the electric force microscopy (EFM) mode that allows to apply a bias voltage at the AFM tip. The tips are Pt-coated, ≈25 nm tip radius, for good conductivity. The scanning rate was 12.5 μm s^{-1}, with a tip setpoint of 30 nN. The surface electric potential and topography of the samples were recorded by the Scanning Kelvin Probe Mode (SKPM), with a tip setpoint of 12 nm and scanning rate of 8 μm s^{-1}.

For the stability tests, several identical samples of SFO were scanned with the electric field and left under atmospheric conditions for a week. Then, one of the samples was covered with Au and measured in FDTR.

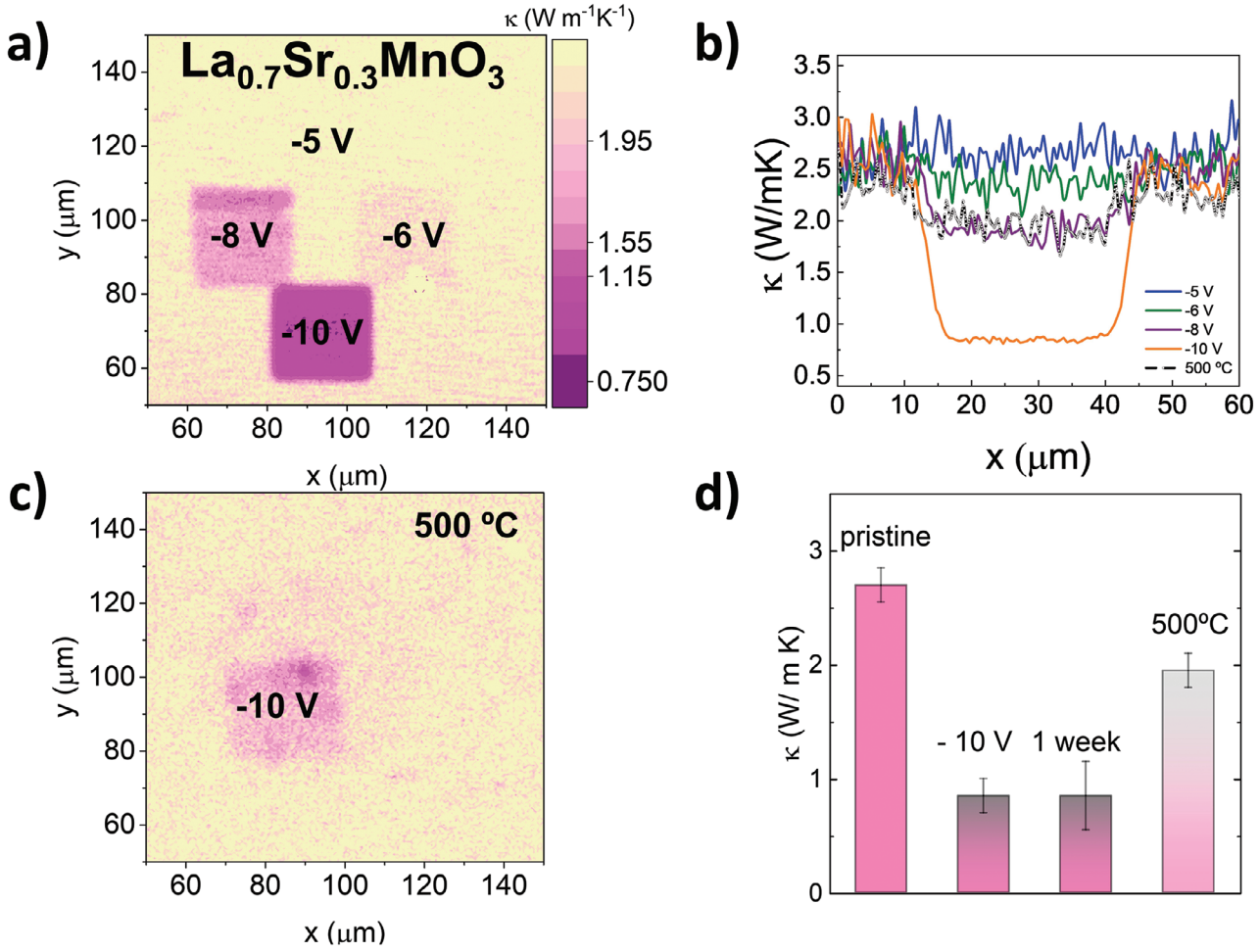

Figure 7. Effect of the electric-field on the local thermal conductivity of Mott–Hubbard oxide $La_{0.7}Sr_{0.3}MnO_3$. Thermal conductivity map of a LSMO film after scanning several areas of 25 × 25 μm^2 with a voltage-biased AFM tip a) and line scans of thermal conductivity along each pad b). c) Retention and reversibility of the written thermal states was probed by following the evolution of the −10 V pads, after 1 week under normal atmospheric conditions, and after thermal annealing at different temperatures, to a maximum of 500 °C. The values of κ are shown in d). Application of −10 V leads to an irreversible transformation of the surface, which cannot be reversed to the original state even after annealing the film at 500 °C.

Another two samples were heated at 200 °C. After that, one of them is covered with Au and measured by FDTR. The other one was used for AFM topography, to verify the recovering of the pristine state, and used for rewriting in the same region that was previously scanned with the electric field. A layer of Au was then deposited and measured thermal conductivity by FDTR. Similar procedure was followed with LSCO and LSMO, at different temperatures as indicated in the paper.

Supporting Information

Supporting Information is available from the Wiley Online Library or from the author.

Acknowledgements

This work received financial support from Ministerio de Ciencia (Spain), project PID2019-104150RB-I00, PID2022-138883NB-I00, TED2021-130930B-I00, and Xunta de Galicia (Centro de investigación do Sistema Universitario de Galicia accreditation 2023–2027, ED431G 2023/03) and the European Union (European Regional Development Fund – ERDF). The research of F.R. received financial support from the Oportunius Program, Xunta de Galicia. N.V.D. acknowledges financial support from MINECO (Spain) through an FPI fellowship (PRE2020-096467). The authors would like to thank the use of the USC Research Infrastructures Area analytical facilities.

Conflict of Interest

The authors declare no conflict of interest.

Data Availability Statement

The data that support the findings of this study are available from the corresponding author upon reasonable request.

Keywords

conductive AFM, thermal conductivity, thermal management, thin films

Received: September 1, 2024
Revised: November 4, 2024
Published online: November 12, 2024

[1] R. Shrestha, Y. Luan, S. Shin, T. Zhang, X. Luo, J. S. Lundh, W. Gong, M. R. Bockstaller, S. Choi, T. Luo, R. Chen, K. Hippalgaonkar, S. Shen, *Sci. Adv.* **2019**, *5*, 3777.
[2] R. Zheng, J. Gao, J. Wang, G. Chen, *Nat. Commun.* **2011**, *2*, 289.
[3] R. Xie, C. T. Bui, B. Varghese, Q. Zhang, C. H. Sow, B. Li, J. T. L. Thong, *Adv. Funct. Mater.* **2011**, *21*, 1602.
[4] J. A. Seijas-Bellido, H. Aramberri, J. Íñiguez, R. Rurali, *Phys. Rev. B* **2018**, *97*, 184306.
[5] C. Liu, Z. Chen, C. Wu, J. Qi, M. Hao, P. Lu, Y. Chen, *ACS Appl. Mater. Interfaces* **2022**, *14*, 46716.
[6] J. F. Ihlefeld, B. M. Foley, D. A. Scrymgeour, J. R. Michael, B. B. McKenzie, D. L. Medlin, M. Wallace, S. Trolier-Mckinstry, P. E. Hopkins, *Nano Lett.* **2015**, *15*, 1791.
[7] E. Langenberg, D. Saha, M. E. Holtz, J. J. Wang, D. Bugallo, E. Ferreiro-Vila, H. Paik, I. Hanke, S. Ganschow, D. A. Muller, L. Q. Chen, G. Catalan, N. Domingo, J. Malen, D. G. Schlom, F. Rivadulla, *Nano Lett.* **2019**, *19*, 7901.
[8] V. Álvarez-Martínez, R. Ramos, V. Leborán, A. Sarantopoulos, R. Dittmann, F. Rivadulla, *ACS Appl. Mater. Interfaces* **2024**, *16*, 15043.
[9] Q. Lu, S. Huberman, H. Zhang, Q. Song, J. Wang, G. Vardar, A. Hunt, I. Waluyo, G. Chen, B. Yildiz, *Nat. Mater.* **2020**, *19*, 655.
[10] Y. Zhang, W. M. Postiglione, R. Xie, C. Zhang, H. Zhou, V. Chaturvedi, K. Heltemes, H. Zhou, T. Feng, C. Leighton, X. Wang, *Nat. Commun.* **2023**, *14*, 2626.
[11] H. A. Tahini, X. Tan, U. Schwingenschlögl, S. C. Smith, *ACS Catal.* **2016**, *6*, 5565.
[12] Q. Yang, H. J. Cho, Z. Bian, M. Yoshimura, J. Lee, H. Jeen, J. Lin, J. Wei, B. Feng, Y. Ikuhara, H. Ohta, *Adv. Funct. Mater.* **2023**, *33*, 2214939.
[13] R. Garcia, A. W. Knoll, E. Riedo, *Nat. Nanotechnol.* **2014**, *9*, 577.
[14] J. A. Dagata, J. Schneir, H. H. Harary, C. J. Evans, M. T. Postek, J. Bennett, *Appl. Phys. Lett.* **1990**, *56*, 2001.
[15] J. A. Dagata, T. Inoue, J. Itoh, K. Matsumoto, H. Yokoyama, *J. Appl. Phys.* **1998**, *84*, 6891.
[16] E. S. Snow, G. G. Jernigan, P. M. Campbell, *Appl. Phys. Lett.* **2000**, *76*, 1782.
[17] X. N. Xie, H. J. Chung, H. Xu, X. Xu, C. H. Sow, A. T. S. Wee, *J. Am. Chem. Soc.* **2004**, *126*, 7665.
[18] R. Held, S. Lüscher, T. Heinzel, K. Ensslin, W. Wegscheider, *Appl. Phys. Lett.* **1999**, *75*, 1134.
[19] S. Masubuchi, M. Arai, T. Machida, *Nano Lett.* **2011**, *11*, 4542.
[20] C. Cen, S. Thiel, G. Hammerl, C. W. Schneider, K. E. Andersen, C. S. Hellberg, J. Mannhart, J. Levy, *Nat. Mater.* **2008**, *7*, 298.
[21] C. Cen, S. Thiel, J. Mannhart, J. Levy, *Science* **2009**, *323*, 1026.
[22] F. Bi, D. F. Bogorin, C. Cen, C. W. Bark, J. W. Park, C. B. Eom, J. Levy, *Appl. Phys. Lett.* **2010**, *97*, 173110.
[23] E. Ferreiro-Vila, S. Blanco-Canosa, I. Lucas del Pozo, H. B. Vasili, C. Magén, A. Ibarra, J. Rubio-Zuazo, G. R. Castro, L. Morellón, F. Rivadulla, *Adv. Funct. Mater.* **2019**, *29*, 1901984.
[24] J. S. Lim, J. Lee, B. J. Lee, Y. J. Kim, H. S. Park, J. Suh, H. H. Nahm, S. W. Kim, B. G. Cho, T. Y. Koo, E. Choi, Y. H. Kim, C. H. Yang, *Sci. Adv.* **2020**, *6*.
[25] S. K. Acharya, R. V. Nallagatla, O. Togibasa, B. W. Lee, C. Liu, C. U. Jung, B. H. Park, J.-Y. Park, Y. Cho, D.-W. Kim, J. Jo, D.-H. Kwon, M. Kim, C. S. Hwang, S. C. Chae, *ACS Appl. Mater. Interfaces* **2016**, *8*, 7902.
[26] U. Aschauer, R. Pfenninger, S. M. Selbach, T. Grande, N. A. Spaldin, *Phys. Rev. B* **2013**, *88*, 054111.
[27] M. Tyunina, O. Pacherova, T. Kocourek, A. Dejneka, *Sci. Rep.* **2021**, *11*, 15247.
[28] E. Sediva, J. L. M. Rupp, *J. Mater. Chem. A* **2023**, *11*, 26752.
[29] O. I. Barkalov, S. V. Zaitsev, V. D. Sedykh, *Solid State Commun.* **2022**, *354*, 114912.
[30] E. Sediva, T. Defferriere, N. H. Perry, H. L. Tuller, J. L. M. Rupp, *Adv. Mater.* **2019**, *31*, 1902493.
[31] D. G. Popescu, N. Barrett, C. Chirila, I. Pasuk, M. A. Husanu, *Phys. Rev. B* **2015**, *92*, 235442.
[32] M. L. Weber, G. Lole, A. Kormanyos, A. Schwiers, L. Heymann, F. D. Speck, T. Meyer, R. Dittmann, S. Cherevko, C. Jooss, C. Baeumer, F. Gunkel, *J. Am. Chem. Soc.* **2022**, *144*, 17966.
[33] W. T. Hong, K. A. Stoerzinger, E. J. Crumlin, E. Mutoro, H. Jeen, H. N. Lee, Y. Shao-Horn, *Top. Catal.* **2016**, *59*, 574.
[34] A. E. Bocquet, A. Fujimori, T. Mizokawa, T. Saitoh, H. Namatame, S. Suga, N. Kimizuka, Y. Takeda, M. Takano, *Phys. Rev. B* **1992**, *45*, 1561.
[35] J. B. Torrance, P. Lacorre, C. Asavaroengchai, R. M. Metzger, *Phys. C Supercond.* **1991**, *182*, 351.
[36] J. Zaanen, G. A. Sawatzky, J. W. Allen, *Phys. Rev. Lett.* **1985**, *55*, 418.
[37] X. Chen, T. Grande, *Chem. Mater.* **2013**, *25*, 3296.
[38] A. Grimaud, O. Diaz-Morales, B. Han, W. T. Hong, Y. L. Lee, L. Giordano, K. A. Stoerzinger, M. T. M. Koper, Y. Shao-Horn, *Nat. Chem.* **2017**, *9*, 457.
[39] A. J. Schmidt, R. Cheaito, M. Chiesa, *Rev. Sci. Instrum.* **2009**, *80*.
[40] X. Wu, J. Walter, T. Feng, J. Zhu, H. Zheng, J. F. Mitchell, N. Biškup, M. Varela, X. Ruan, C. Leighton, X. Wang, *Adv. Funct. Mater.* **2017**, *27*, 1704233.
[41] E. Langenberg, E. Ferreiro-Vila, V. Leborán, A. O. Fumega, V. Pardo, F. Rivadulla, *APL Mater.* **2016**, *4*, 104815.